We are IntechOpen, the world's leading publisher of Open Access books Built by scientists, for scientists

6,900
Open access books available

186,000
International authors and editors

200M
Downloads

Our authors are among the

154
Countries delivered to

TOP 1%
most cited scientists

12.2%
Contributors from top 500 universities

WEB OF SCIENCE™

Selection of our books indexed in the Book Citation Index in Web of Science™ Core Collection (BKCI)

Interested in publishing with us?
Contact book.department@intechopen.com

Numbers displayed above are based on latest data collected.
For more information visit www.intechopen.com

3

Electron Holography of Magnetic Materials

Takeshi Kasama[1],
Rafal E. Dunin-Borkowski[2] and Marco Beleggia[1]
[1]*Technical University of Denmark,*
[2]*Forschungszentrum Jülich,*
[1]*Denmark*
[2]*Germany*

1. Introduction

Transmission electron microscopy (TEM) involves the use of high-energy (60-3000 keV) electrons that have passed through a thin specimen to record images, diffraction patterns or spectroscopic information from a region of interest. Many different TEM techniques have been developed over the years into highly sophisticated methodologies that have found widespread application across scientific disciplines. Because the TEM has an unparalleled ability to provide structural and chemical information over a range of length scales down to atomic dimensions, it has developed into an indispensable tool for scientists who are interested in understanding the properties of nanostructured materials and in manipulating their behavior (Smith, 2007).

State-of-the-art TEMs are now equipped with spherical and chromatic aberration correctors and can provide interpretable image resolutions of 0.05 nm (Erni et al., 2009). However, in addition to conventional TEM techniques that can be used to provide structural and compositional information about materials, the TEM also allows magnetic and electrostatic fields in specimens to be imaged with nanometer spatial resolution. One of the most powerful techniques for providing this information is electron holography, which was originally proposed as a means to compensate for lens aberrations and to improve electron microscope resolution (Gabor, 1949). Electron holography is still the only technique that provides direct access to the phase shift of the electron wave that has passed through a thin specimen, in contrast to more conventional TEM techniques that record only spatial distributions of image intensity.

Electron holography has only recently become widely available on commercial electron microscopes. The earliest studies using electron holography were restricted by the limited brightness and coherence of the tungsten filaments that were used as electron sources (Haine & Mulvey, 1952). The availability of high brightness, stable, coherent field emission electron guns now allows electron holography to be applied to a wide variety of materials such as quantum well structures, magnetic thin films, semiconductor devices, natural rocks and biominerals.

Although there are several forms of electron holography, including in-line and scanning TEM-based electron holography (Cowley, 1992), the most commonly-used form is the TEM mode of off-axis electron holography, which involves using an electrostatic biprism that is inserted into the microscope column perpendicular to the electron beam (Möllenstedt & Düker, 1956). As described in detail below, the application of a voltage to the biprism results in overlap of the electron wave to create an interference fringe pattern. Other forms of electron holography are described elsewhere (e.g., Cowley & Spence, 1998).

Off-axis electron holography can be divided further into two modes: (i) High-resolution electron holography, in which the interpretable resolution in a high-resolution TEM image can be improved by the use of phase plates to correct for microscope lens aberrations (Lichte, 1991; Lehmann et al., 1999) and (ii) Medium-resolution electron holography, in which magnetic and electrostatic fields in materials can be studied quantitatively, usually with nanometer spatial resolution (Tonomura, 1992; Dunin-Borkowski et al., 2004). Some of the most successful early examples of the application of medium-resolution electron holography include the experimental confirmation of magnetic flux quantization in superconducting toroids (i.e., the Aharonov-Bohm effect) and the study of magnetic flux vortices in superconductors (Tonomura et al., 1986; Matsuda et al, 1989). Here we concentrate on more recent applications of medium-resolution electron holography for the study of magnetic materials.

This chapter begins with an outline of the basis and requirements for electron holography and the procedures that are typically used to obtain amplitude and phase information from electron holograms, including microscope calibrations for magnetic studies and the practical steps that are required to extract the magnetic contribution to the signal from a reconstructed phase image. We then provide selected examples of the application of electron holography to the characterization of magnetic domain structures in nanostructured materials. We describe a novel approach for measuring the magnetic moment of a chosen nanocrystal quantitatively, before discussing future opportunities for the development and application of electron holography for the study of magnetic materials and devices.

2. Basis of off-axis electron holography

Off-axis electron holography in the TEM involves the examination of a thin specimen using a highly coherent field emission electron source. A schematic diagram showing the typical electron-optical configuration is shown in Fig. 1a. The region of interest is positioned so that it covers approximately half the field of view. A biprism (a thin conducting wire), which is usually located close to the first image plane, has a positive voltage applied to it in order to overlap a "reference" electron wave that has passed through vacuum with the electron wave that has passed through the specimen. The overlap region contains interference fringes and an image of the specimen, in addition to Fresnel fringes originating from the edge of the biprism wire (Figs 1b-e). The electron-optical configuration is equivalent to the use of two electron sources S_1 and S_2, as shown in Fig. 1a (Dunin-Borkowski et al., 2004). By applying a larger voltage to the biprism wire, the separation of the two virtual sources and the width of the overlap region W increase (Figs 1b-d), placing a greater constraint on the spatial coherence of the source required to maintain sufficient interference fringe contrast.

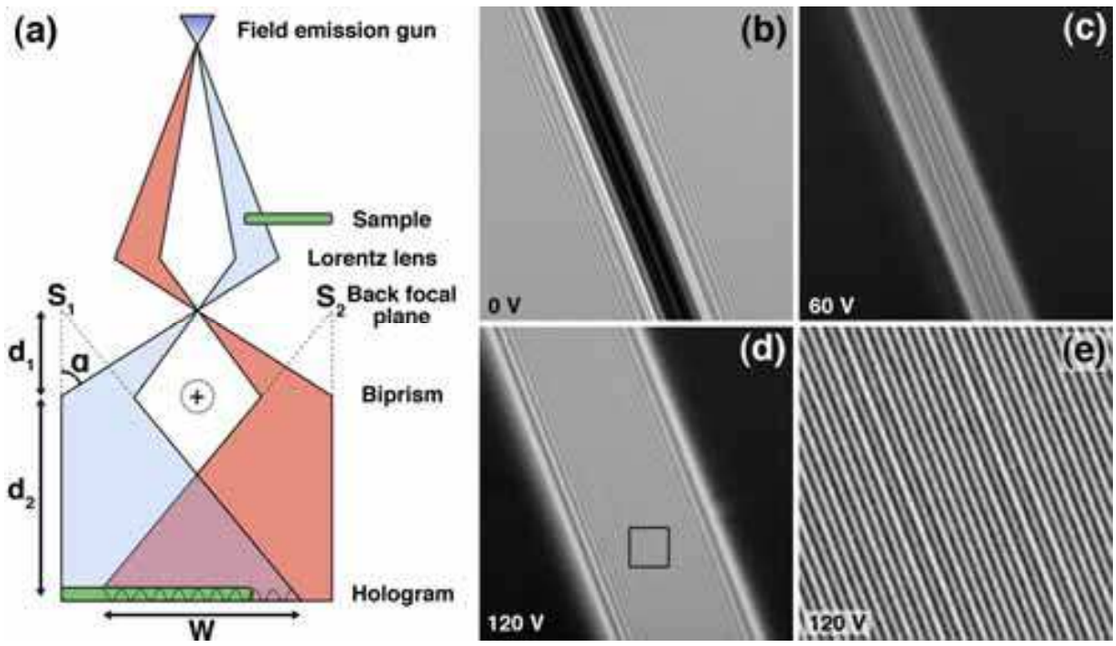

Fig. 1. (a) Schematic diagram of the setup for off-axis electron holography. The symbols are defined in the text. (b-e) Interference fringe patterns (electron holograms) recorded using biprism voltages of (b) 0 V, (c) 60 V and (d,e) 120 V. In (b), only Fresnel fringes from the edges of the biprism wire are visible. Image (e) corresponds to the box marked in (d). The field of view in (b)-(d) is 916 nm.

2.1 Intensity distribution in bright-field TEM images and electron holograms

In coherent image formation in the TEM, the electron wavefunction in the image plane can be written in the form

$$\psi_i(\mathbf{r}) = A_i(\mathbf{r})\exp[i\phi_i(\mathbf{r})] \tag{1}$$

where $\mathbf{r}$ is a two-dimensional vector in the plane of the sample, and A and ϕ refer to amplitude and phase, respectively. In a conventional bright-field TEM image, the intensity distribution imaged on a recording medium is given by the expression

$$I(\mathbf{r}) = \left|A_i(\mathbf{r})\right|^2 \tag{2}$$

and all information that relates directly to the phase is lost. In contrast, the intensity distribution in an off-axis electron hologram can be obtained by considering the addition of a tilted plane reference wave to the complex specimen wave in the form

$$I_{hol}(\mathbf{r}) = \left|\psi_i(\mathbf{r}) + \exp[2\pi i \mathbf{q}_c \bullet \mathbf{r}]\right|^2 \tag{3}$$

where the tilt of the reference wave is specified by the two-dimensional reciprocal space vector $\mathbf{q} = \mathbf{q}_c$. By combining this expression with Eq. 1, it can be rewritten in the form

$$I_{hol}(\mathbf{r}) = 1 + A_i^2(\mathbf{r}) + 2A_i(\mathbf{r})\cos[2\pi i \mathbf{q}_c \bullet \mathbf{r} + \phi_i(\mathbf{r})]\,, \tag{4}$$

highlighting the fact that the intensity in an electron hologram consists of three separate contributions: the reference image intensity, the specimen image intensity and a set of cosinusoidal fringes, whose local phase shifts and amplitudes are equivalent to the phase and amplitude, respectively, of the electron wavefunction in the image plane. An experimental electron hologram of a specimen that contains magnetic crystals is shown in Fig. 2a, alongside a vacuum reference hologram (Fig. 2b) and a magnified region of the specimen hologram (Fig. 2c). The amplitude and phase shift of the specimen wave are recorded in the intensity and position, respectively, of the holographic interference fringes.

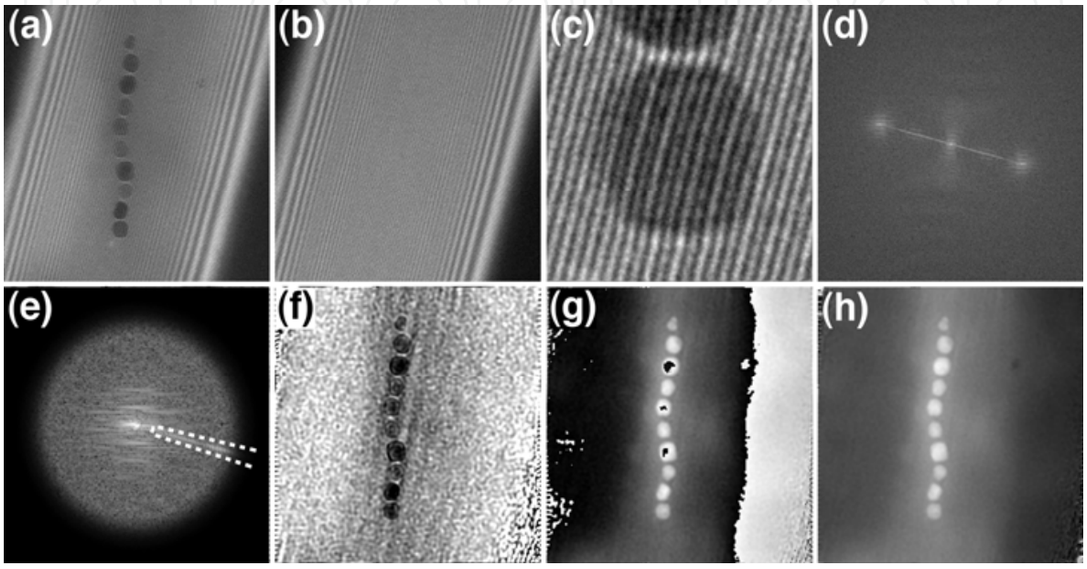

Fig. 2. Sequence of processing steps required to convert a recorded electron hologram into an amplitude and phase image. (a) Experimentally acquired hologram of a region of interest (a chain of magnetite crystals in a magnetotactic bacterium). Coarser fringes, resulting from Fresnel diffraction at the edges of the biprism wire, are visible on either side of the overlap region. The overlap width and holographic interference fringe spacing are 650 and 3.3 nm, respectively. The field of view is 725 nm. (b) Vacuum reference hologram acquired immediately after the specimen hologram. (c) Magnified region of the specimen hologram, showing changes in the positions of interference fringes in a particle. (d) Fourier transform of the electron hologram shown in (a), containing a centerband, two sidebands and a diagonal streak resulting from the presence of Fresnel fringes in the hologram. (e) One of the sidebands extracted from the Fourier transform, shown after applying a circular mask with smooth edges to reduce its intensity radially to zero. If required, the streak from the Fresnel fringes can be removed in a similar manner, by assigning a value of zero to pixels inside the region shown by the dashed line. Inverse Fourier transformation of the sideband is used to provide a complex image wave, which is then displayed in the form of (f) an amplitude image and (g) a modulo 2π phase image. Phase unwrapping algorithms are used to remove the 2π phase discontinuities from (g) to yield the final unwrapped phase image shown in (h).

2.2 Reconstruction of electron holograms

In order to extract phase and amplitude information from an electron hologram, it is usually first Fourier transformed. Based on Eq. 4, the Fourier transform of an electron hologram can be written in the form

$$FT[I_{hol}(\mathbf{r})] = \delta(\mathbf{q}) + FT[A_i{}^2(\mathbf{r})] + \delta(\mathbf{q}+\mathbf{q_c}) \otimes FT[A_i(\mathbf{r})\exp[i\phi_i(\mathbf{r})]]$$

$$+\delta(\mathbf{q}-\mathbf{q_c}) \otimes FT[A_i(\mathbf{r})\exp[-i\phi_i(\mathbf{r})]] \quad (5)$$

Equation 5 describes a peak at the origin of reciprocal space corresponding to the Fourier transform of the reference image, a second peak centered at the origin corresponding to the Fourier transform of a conventional bright-field TEM image of the sample, a peak centered at $\mathbf{q} = \mathbf{-q_c}$ corresponding to the Fourier transform of the desired image wavefunction and a peak centered at $\mathbf{q} = \mathbf{+q_c}$ corresponding to the Fourier transform of the complex conjugate of the wavefunction. Figure 2d shows the Fourier transform of the hologram shown in Fig. 2a. In order to recover the complex electron wavefunction, one of the two "sidebands" in the Fourier transform is selected (Fig. 2e) and then inverse Fourier transformed. The amplitude and phase of the complex image wave are calculated by using the expressions

$$A = \sqrt{\mathrm{Re}^2 + \mathrm{Im}^2} \quad (6)$$

$$\phi = \tan^{-1}\left(\frac{\mathrm{Im}}{\mathrm{Re}}\right) \quad (7)$$

where Re and Im are the real and imaginary parts of the complex image wavefunction, respectively. Figures 2f and 2g show the resulting amplitude and phase images, respectively. The amplitude image is similar to an energy-filtered bright-field TEM image since the contribution of inelastic scattering to holographic interference fringe formation is negligible (Verbeeck et al., 2011). The phase image is initially calculated modulo 2π, meaning that 2π phase discontinuities appear at positions where the phase shift exceeds this amount (Fig. 2g). If required, the phase image can then be "unwrapped" by using suitable algorithms (e.g., Takeda et al., 1982), as shown in Fig. 2h.

In Fig. 2d, the streak from the "centerband" toward the sidebands is attributed to the presence of Fresnel fringes from the biprism wire, which have a range of spacings. The contribution of this streak to the sideband can lead to artifacts in reconstructed amplitude and phase images and can be minimized by masking it from the Fourier transformtion before inverse Fourier transformation (Fig. 2e). Alternatively, the Fresnel fringes can be eliminated by introducing a second biprism close to a different image plane in the microscope column (Yamamoto et al., 2004; Harada et al., 2005).

As phase information is stored in the lateral displacements of holographic interference fringes, long-range phase modulations arising from inhomogeneities in the charge and thickness of the biprism wire, as well as from lens distortions and charging effects (e.g., at apertures), can introduce artifacts into the reconstructed wavefunction. In order to take these effects into account, a reference hologram is usually obtained from vacuum alone by removing the specimen from the field of view without changing the electron-optical parameters of the microscope (Fig. 2b). Correction is then possible by performing a complex division of the specimen wavefunction by the vacuum wavefunction in real space and calculating the phase of the resulting complex wavefunction to obtain the distortion-free phase of the image wave.

2.3 Magnetic and mean inner potential contributions to the phase shift

The phase shift recorded using electron holography is sensitive to both the electrostatic potential and the in-plane component of the magnetic induction in the specimen. Neglecting dynamical diffraction (i.e., assuming that the specimen is thin and weakly diffracting), the phase shift can be written in the form

$$\phi(x,y) = \phi_e(x,y) + \phi_m(x,y) = C_E \int_{-\infty}^{+\infty} V(x,y,z)dz - \frac{e}{\hbar}\int_{-\infty}^{+\infty} A_z(x,y,z)dz \tag{8}$$

where V is the electrostatic potential, A_z is the component of the magnetic vector potential parallel to the electron beam direction and

$$C_E = \left(\frac{2\pi}{\lambda}\right)\left(\frac{E+E_0}{E(E+2E_0)}\right) \tag{9}$$

is a constant that depends on the microscope accelerating voltage $U=E/e$. In Eq. 9, λ is the (relativistic) electron wavelength and E_0=511 keV is the rest mass energy of the electron. C_E is a constant that depends on the microscope accelerating voltage and takes values of 1.01×10^7, 8.64×10^6 and 6.53×10^6 rad/Vm at accelerating voltages of 80, 120 and 300 kV, respectively. If no external charge distributions or applied electric fields are present within or around the specimen, then the only electrostatic contribution to the phase shift originates from the mean inner potential V_0 of the material coupled with thickness variations of the specimen (most importantly at its edge):

$$\phi_e(x,y) = C_E V_0 t(x,y) \tag{10}$$

where $t(x,y)$ is the specimen thickness. If the specimen has uniform composition, then the electrostatic contribution to the phase shift is proportional to the local specimen thickness at position (x,y). Alternatively, should the thickness be known independently, ϕ_e can be used to provide a measurement of the local mean inner potential.

The magnetic contribution to the phase shift carries information about the magnetic flux. The difference between its value at two arbitrary points in a phase image at coordinates (x_1,y_1) and (x_2,y_2)

$$\Delta\phi_m = \phi_m(x_1,y_1) - \phi_m(x_2,y_2) = -\frac{e}{\hbar}\int_{-\infty}^{+\infty} A_z(x_1,y_1,z)dz + \frac{e}{\hbar}\int_{-\infty}^{+\infty} A_z(x_2,y_2,z)dz \tag{11}$$

can be written in the form of a loop integral

$$\Delta\phi_m = -\frac{e}{\hbar}\oint \mathbf{A}\cdot d\mathbf{l} \tag{12}$$

for a rectangular loop formed by two parallel electron trajectories crossing the sample at coordinates (x_1,y_1) and (x_2,y_2) and joined, at infinity, by segments perpendicular to the trajectories. By virtue of Stokes' theorem,

$$\Delta\phi_m = \frac{e}{\hbar}\iint \mathbf{B}\cdot\hat{\mathbf{n}}\,dS = \frac{\pi}{\phi_0}\Phi(S) \tag{13}$$

where $\phi_0 = h/2e = 2.07\times10^{-15}$ Tm² is a flux quantum. The phase difference between any two points in a phase image is therefore a measure of the magnetic flux through the whole region of space bounded by two electron trajectories crossing the sample at the positions of these two points. A graphical representation of the magnetic flux distribution throughout the sample can therefore be obtained by adding contours to a recorded phase image. A phase difference of 2π in such an image corresponds to an enclosed magnetic flux of 4.14×10^{-15} Tm². The relationship between the magnetic contribution to the phase shift and the magnetic induction can be established by considering the gradient of ϕ_m, which takes the form

$$\vec{\nabla}\phi_m(x,y) = \frac{e}{\hbar}\left[B_y^p(x,y), -B_x^p(x,y)\right] \tag{14}$$

where

$$B_j^p(x,y) = \int_{-\infty}^{+\infty} B_j(x,y,z)dz \tag{15}$$

are the components of the magnetic induction perpendicular to the incident electron beam direction projected in the beam direction. In the special case where (i) stray fields surrounding the sample can be neglected, (ii) the sample has a constant thickness and (iii) the magnetic induction does not vary with z within the specimen, Eq. 14 can be rewritten in the simplified form

$$\vec{\nabla}\phi_m(x,y) = \frac{et}{\hbar}\left[B_y(x,y), -B_x(x,y)\right], \tag{16}$$

in which there is direct proportionality between the magnetic contribution to the phase gradient and the magnetic induction. Equation 16 has a limited validity, however, and must be used with caution if the aim is to quantify the magnetic field strength and its direction on a local scale. For visualization purposes, it can be useful to relate the spacing and direction of phase contours to the direction of the projected magnetic field within the field of view.
It should be noted that the separation of electrostatic and magnetic contributions to the phase shift is almost always mandatory in order to obtain quantitative magnetic information from a phase image. The few instances when this extra step may be avoided include the special case of magnetic domains in a thin film of constant thickness (far from the specimen edge) and a measurement scheme for quantifying magnetic moments that is described in section 4 below.

2.4 Phase shift of an isolated magnetic nanoparticle

Analytical expressions for the phase shift of an isolated spherical magnetic particle, based on Eq. 8, can be derived for a uniformly magnetized sphere of radius a, magnetic induction $B_\perp$ (along y) and mean inner potential V_0 in the form (de Graef et al., 1999)

$$\phi(x,y)\Big|_{x^2+y^2\le a^2} = 2C_E V_0\sqrt{a^2-(x^2+y^2)} + \frac{2}{3}\left(\frac{e}{\hbar}\right)B_\perp a^3\left(\frac{x}{x^2+y^2}\right)\left\{1-\left[1-\left(\frac{x^2+y^2}{a^2}\right)\right]^{\frac{3}{2}}\right\} \tag{17}$$

$$\phi(x,y)\Big|_{x^2+y^2>a^2} = \frac{2}{3}\left(\frac{e}{\hbar}\right)B_{\perp}a^3\left(\frac{x}{x^2+y^2}\right). \tag{18}$$

Graphical representations of Eqs 17 and 18 are shown in Fig. 4 below for a uniformly-magnetized 50-nm-diameter spherical particle of cobalt, on the assumption that V_0 =17.8 V and $B_{\perp}$=1.8 T. The total phase shift is the sum of mean inner potential and magnetic contributions. For a line profile across the center of the particle in a direction perpendicular to $B_{\perp}$, the expressions reduce to

$$\phi(x)\Big|_{|x|\le a} = 2C_E V_0\sqrt{a^2-x^2} + \frac{2}{3}\left(\frac{e}{\hbar}\right)B_{\perp}\left(\frac{a^3-(a^2-x^2)^{\frac{3}{2}}}{x}\right) \tag{19}$$

$$\phi(x)\Big|_{|x|>a} = \frac{2}{3}\left(\frac{e}{\hbar}\right)B_{\perp}\left(\frac{a^3}{x}\right) \tag{20}$$

which can be used for measurements of the in-plane magnetic induction and mean inner potential of the particle by least-squares fitting (an example is shown in section 3.1.1.1). The magnitude of the difference between the maximum and minimum values of the magnetic contribution to the phase shift across a uniformly magnetized sphere of radius a can be determined from Eqs 19 and 20 to be

$$\left|\Delta\phi_m\right| = 2.044\left(\frac{e}{\hbar}\right)\left|B_{\perp}\right|a^2 . \tag{21}$$

For a uniformly-magnetized infinite cylinder of radius a, the equivalent expression is

$$\left|\Delta\phi_m\right| = \pi\left(\frac{e}{\hbar}\right)\left|B_{\perp}\right|a^2 . \tag{22}$$

2.5 Requirements for off-axis electron holography

In order to provide a highly coherent electron beam, a field emission gun electron source is essential. Although no electron source is perfectly coherent, either spatially or temporally, the degree of coherence must be such that an interference fringe pattern of sufficient quality can be recorded within a reasonable acquisition time, during which specimen and/or beam drift must be negligible. It is common practice to adjust the condenser lens astigmatism to make the beam illumination elongated in the direction perpendicular to the biprism wire. Coherence is then maximized in the elongation direction, while the electron flux is maximized in the region of interest. The elongation direction of the illumination has to be aligned at exactly 90° to the biprism wire, as a slight misalignment can lead to a dramatic decrease in interference fringe contrast. In order to maximize fringe visibility, a small spot size, small condenser aperture size, parallel illumination and a low extraction voltage are usually required. In practice, a balance between coherence, intensity and acquisition time must be achieved.

When characterizing magnetic materials, the microscope objective lens is usually turned off because it creates a large (>2 T) magnetic field at the position of the specimen. Instead, a

non-immersion Lorentz lens is used as the primary imaging lens. The Lorentz lens is located within the lower pole piece of the objective lens and allows specimens to be imaged at relatively high magnifications in magnetic-field-free conditions. Although the spherical aberration coefficient C_S of the Lorentz lens is large (e.g., 8400 mm for an FEI Titan microscope (Phatak et al., 2008)), resulting in a point resolution of ~2 nm, magnetic fields in most specimens of interest are relatively slowly varying and the spatial resolution for magnetic characterization using electron holography is often limited primarily by a combination of interference fringe spacing and signal to noise considerations.

The electron biprism, which is normally either a Au-coated glass fiber or a Pt wire with a diameter of ~1 μm, is usually positioned in place of one of the selected-area apertures, close to the first image plane. The optimal position for the biprism in the microscope column has been discussed by Lichte (1996). It should be noted that the biprism cannot be located exactly in an intermediate image plane (Smith & McCartney, 1998). Hence, a readjustment of the electron optics is required in most TEMs. For example, the first intermediate lens may be over-excited and the objective lens (or Lorentz lens) then refocused to place the image below the biprism plane (Smith & McCartney, 1998). Lateral movement and rotation of the biprism is a useful feature, especially for studying magnetic materials.

The most common medium used to record electron holograms is a charge-coupled device (CCD) camera, which provides linear output over a large dynamic range and a high detection quantum efficiency. Digital recording is also convenient for subsequent computer image processing, including reconstruction of holograms. A phase sensitivity of $2\pi/100$ can be achieved by the use of digital recording and processing (de Ruijter & Weiss, 1993), in place of the use of an optical bench as a Mach-Zender interferometer (Tonomura, 1992).

2.6 Imaging parameters

Three coupled experimental parameters affect the quality of final reconstructed phase images significantly: (i) overlap width, (ii) interference fringe spacing and (iii) interference fringe visibility. In general, the application of a higher biprism voltage results in a larger overlap width, a finer interference fringe spacing and a decrease in fringe contrast.

2.6.1 Overlap width

The application of a voltage to a biprism wire results in an overlap width that is given by the expression

$$W = 2\left(\frac{d_1 + d_2}{d_1}\right)\left(\alpha\frac{d_1 d_2}{d_1 + d_2} - R\right) \tag{23}$$

where d_1 is the distance between the focal plane and the biprism, d_2 is the distance between the biprism and the image plane, R is the radius of the biprism wire and α is the deflection angle, as defined in Fig. 1a. A thinner biprism wire can result in a larger overlap width for a given interference fringe spacing and can have fewer Fresnel fringes from the edge of the wire. The overlap width varies linearly with biprism voltage, as shown in Figs 3a and d for an FEI Titan TEM operated at 300 kV, and typically takes a value of between 0.5 and 1.5 μm when using the Lorentz lens as the primary imaging lens of the microscope. The overlap width and the interference fringe spacing can be changed by adjusting the strength of the projector lenses after the biprism either with or without slightly exciting the objective lens (Frost et al., 1996; Sickmann et al., 2011).

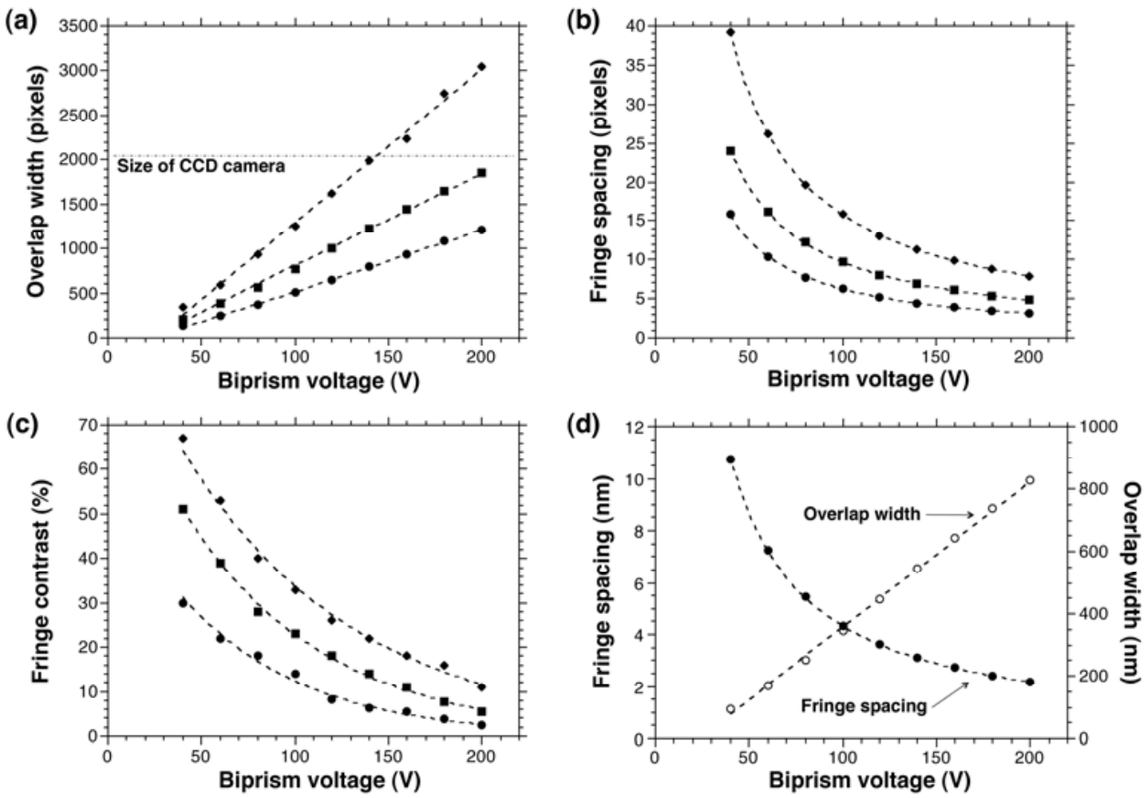

Fig. 3. Measured dependence of (a) overlap width, (b) interference fringe spacing and (c) interference fringe visibility recorded at indicated magnifications of 1450x (circles), 2250x (squares) and 3700x (diamonds) on an FEI Titan 80-300ST TEM operated at 300 kV in Lorentz mode. A Gatan model 894 2K (2048×2048 pixel) UltraScan 1000FT CCD camera mounted in a Gatan imaging filter was used. (d) Interference fringe spacing (filled circles) and overlap width (open circles) in nm plotted as a function of biprism voltage.

2.6.2 Interference fringe spacing

The interference fringe spacing is inversely proportional to the biprism voltage and is given by the expression

$$s = \lambda \left(\frac{d_1 + d_2}{2\alpha d_1} \right), \tag{24}$$

as shown in Fig. 3b for an FEI Titan TEM. Fringe spacings of between 2 and 5 nm are typically used for examining magnetic materials, with a spatial resolution in the final phase image that is presently, at best, approximately three times the measured fringe spacing (Völkl & Lichte, 1990).

2.6.3 Interference fringe visibility

The fringe visibility is one of the most important parameters for electron holography, as it can determine the phase resolution (Lichte, 2008), which is given by the expression

$$\phi_{\min} = \frac{SNR}{\mu}\sqrt{\frac{2}{N_{el}}} \tag{25}$$

where the fringe visibility

$$\mu = \left(\frac{I_{\max} - I_{\min}}{I_{\max} + I_{\min}}\right), \tag{26}$$

SNR is the signal-to-noise ratio in the hologram, N_{el} is the number of electrons collected per pixel and I_{max} and I_{min} are the maximum and minimum intensities of the interference fringes, respectively (Völkl et al., 1995). Figure 3c shows measurements of fringe visibility plotted as a function of biprism voltage for an FEI Titan TEM operated at different magnifications. The difference between the graphs is attributed to the modulation transfer function of the CCD camera, suggesting that the use of a higher magnification can result in better phase resolution, although the field of view then becomes smaller. The recommended number of pixels per interference fringe on a CCD camera is generally chosen to be at least four (Smith & McCartney, 1998). The number of electrons per pixel in a recorded electron hologram is usually at least 100-500 for an acquisition time of 2-8 sec. If the biprism wire and the specimen are stable enough, then a longer acquisition time can be used (Cooper et al., 2007). Furthermore, if two or more biprisms are used simultaneously, then there is more flexibility to control the overlap width, interference fringe spacing and biprism rotation angle independently, as well as to eliminate Fresnel fringes from the recorded image wave (Harada et al., 2006).

2.7 Separation of magnetic and mean inner potential contributions to the phase

Although measurements of the local value of the mean inner potential can be used to provide useful information about the morphology or chemical composition of a specimen (Dunin-Borkowski et al., 2004), its contribution to the phase shift is generally detrimental for studies of magnetic materials using electron holography. In particular, it can be much larger than the magnetic contribution to the phase shift for small (sub-50-nm) magnetic nanocrystals. Figure 4 shows simulations of the mean inner potential and magnetic contributions to the phase shift for a 50-nm-diameter Co crystal that is uniformly magnetized. Although the particle is in a single domain state, the mean inner potential dominates the recorded phase image. Separation of the desired magnetic contribution from the total phase shift is then essential.

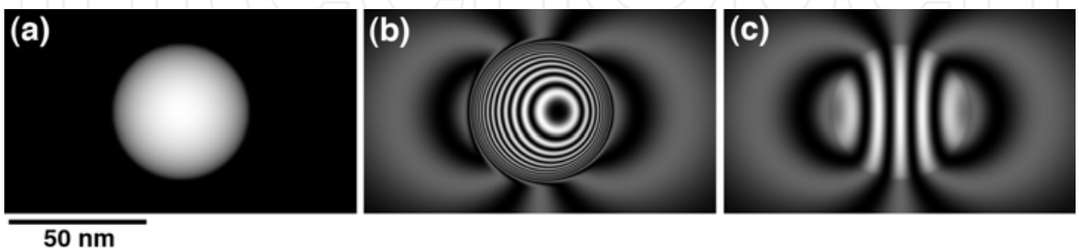

Fig. 4. Simulations of the phase shift of a 50-nm-diameter Co (B=1.8 T; V_0=17.8 V) spherical particle, which is uniformly magnetized in the vertical direction. (a) Thickness map. (b) Total phase shift. (c) Magnetic contribution to the phase shift alone. In (b) and (c), the cosine of 12 times the phase is shown.

In principle, the most accurate way of achieving this separation involves turning the specimen over after acquiring a hologram and acquiring a second hologram from the same region, as shown in Fig. 5. The two holograms are aligned after flipping one of them over digitally (Fig. 5a). Then, their sum and difference are used to determine twice the mean inner potential and twice the magnetic contribution to the phase shift, respectively. The mean inner potential contribution can be subtracted from all subsequent phase images acquired from the same region (Fig. 5b), followed by adding phase contours and colors to form final magnetic induction maps. A degree of smoothing of the final phase images is often used to remove statistical noise and artifacts resulting from misalignment of the pairs of phase images.

An alternative method, which is often more practical, involves performing a magnetization reversal experiment *in situ* in the microscope and then selecting pairs of holograms that differ only in the magnetization direction in the specimen. The addition of two phase images, in which the specimen is oppositely magnetized, provides twice the mean inner potential contribution to the phase. Magnetization reversal can be performed by using either a magnetizing TEM specimen holder or the vertical magnetic field of the conventional microscope objective lens and tilting the specimen. In the latter case, the objective lens can be turned off and the specimen is tilted back to the horizontal before acquiring each hologram. This approach is only applicable if the magnetization in the specimen reverses perfectly. If this is not the case, then reversal measurements may need to be repeated multiple times so that non-systematic differences between reversed images are averaged out.

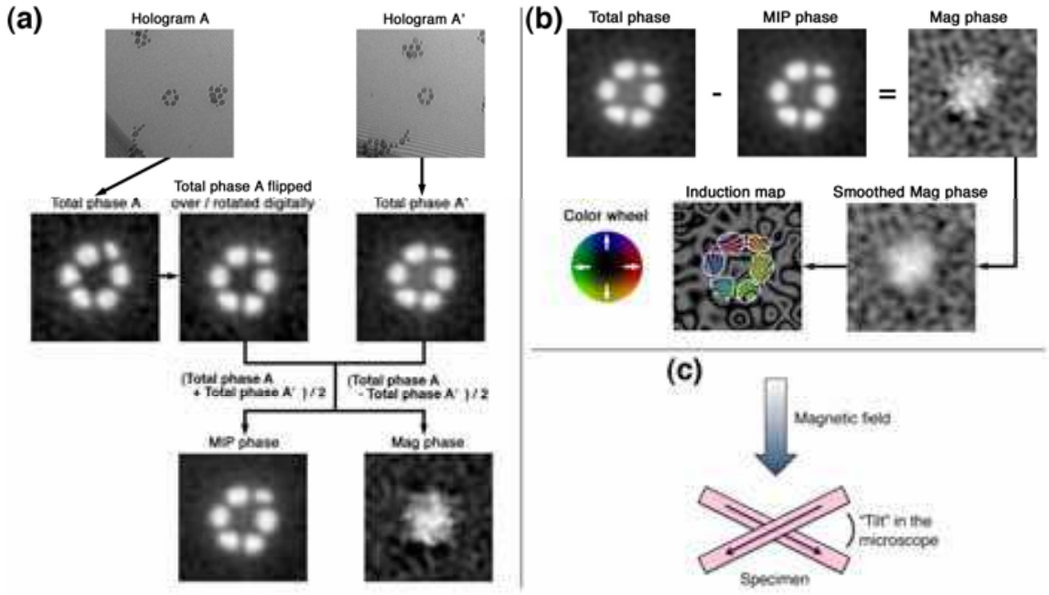

Fig. 5. Experimental procedure used to obtain (a) the mean inner potential (MIP) contribution to the phase shift and (b) the magnetic (Mag) contribution to the phase shift and the final induction map for a self-assembled ring of 25-nm-diameter Co crystals (Kasama et al., 2008). The induction map in (b) shows the cosine of 96 times the magnetic contribution to the phase. The color wheel shows the direction of the projected induction in each crystal. (c) Schematic diagram showing the use of *in situ* tilting of a specimen in the vertical magnetic field of the partially excited microscope objective lens to perform a magnetization reversal experiment. Adapted from Kasama et al. (2007).

If the magnetization in the specimen does not reverse exactly and if the specimen cannot be turned over during an experiment, then it may be possible to generate an "artificial" mean inner potential map either from a t/λ map (where t is the specimen thickness and λ is the inelastic mean free path) (Egerton, 1996) or from a high-angle annular dark-field image. The constant of proportionality between the thickness map and the mean inner potential contribution to the phase can be determined by least-squares fitting to data collected near the specimen edge, where the magnetic contribution to the phase shift is smallest (Harrison et al., 2002). This method may not be applicable in the presence of strong diffraction contrast or if the specimen contains several materials with different compositions. In this situation, the use of two different microscope accelerating voltages or a phase image acquired above the Curie or Néel temperature of the specimen (Loudon et al., 2002) may provide an alternative approach.

2.8 Calibration of the magnetic field of the objective lens

The objective lens of the microscope can generate a magnetic field of up to ~2 T in the direction of the electron beam, which would saturate the magnetization in most samples in this direction. Hence, for magnetic studies, the objective lens is usually either turned off or excited slightly to apply a chosen magnetic field to the sample. Figure 6 shows a Hall probe calibration of the vertical magnetic field at the specimen position in an FEI Titan TEM operated at 300 kV, plotted as a function of normalized objective lens current. Additional lenses such as the mini-condenser and Lorentz lens also affect the magnetic field at the position of the specimen slightly. In practice, however, since the mini-condenser lens setting is fixed and the Lorentz lens is adjusted only slightly for focusing, the resulting change in the magnetic field at the specimen can be as small as ±1 Oe.

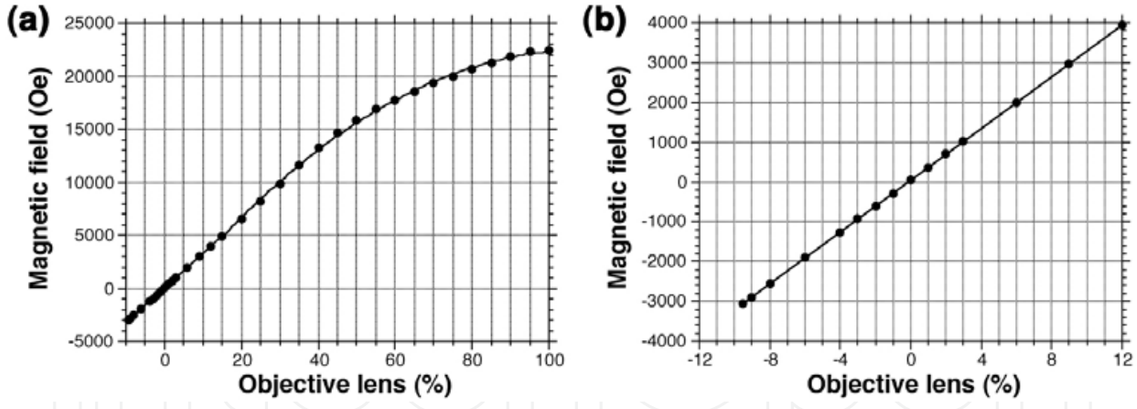

Fig. 6. Hall probe calibration of the magnetic field in the specimen plane for an FEI Titan 80-300ST TEM operated at 300 kV, plotted as a function of normalized objective lens current. In this condition, zero field is obtained at an objective lens current of -0.124%.

3. Applications of electron holography to magnetic materials

3.1 Magnetic properties of magnetite

Magnetite (Fe_3O_4) was the first magnetic material to be exploited by humankind and is one of the most important magnetic minerals in geological and biological systems (Dunlop & Özdemir, 1997). Recently, magnetite nanoparticles have been identified as promising candidates for medical applications such as targeted drug delivery (Pankhurst et al., 2009).

Here, we present two examples of the characterization of the magnetic properties of magnetite using electron holography.

3.1.1 Low-temperature magnetic properties

The Verwey transition in magnetite, which is a first-order crystallographic phase transition, has been studied extensively since its discovery (Verwey, 1939) because of its enormous impact on the magnetic and other physical properties of the material (Walz, 2001). The Verwey transition is associated with an order-of-magnitude increase in magnetocrystalline anisotropy and a change in magnetic easy axis from cubic <111> to monoclinic [001] below ~120 K. Although numerous studies have suggested that magnetic domain walls in magnetite can interact with the ferroelastic twin walls that form at low temperature (e.g., Smirnov & Tarduno, 2002), no direct evidence for such interactions has previously been presented. Here, for low-temperature electron holography experiments, a liquid-nitrogen-cooled TEM specimen holder (~90 K) was used.

3.1.1.1 Single-domain magnetite

Experimental results obtained using electron holography from an isolated 50-nm-diameter single crystal of magnetite from a bacterial cell are shown in Fig. 7. Figure 7a shows a high-resolution TEM image of the crystal, which is elongated slightly in the [111] direction. The three-dimensional morphology of the same crystal, determined using high-angle annular dark-field electron tomography, is shown in Fig. 7b. Magnetic induction maps were recorded using electron holography with the crystal in magnetic-field-free conditions, both at room temperature (Fig. 7c) and at 90 K (Fig. 7d). The magnetic contribution to the phase shift was determined by performing a series of *in situ* magnetization reversal experiments. Both induction maps show uniformly-magnetized single domain states, including a characteristic return flux resembling that of an isolated magnetic dipole, with the remanent magnetization direction making a large angle to the applied field direction. At room temperature, the phase contours in the crystal make an angle of ~20° to its [111] elongation direction (Fig. 7c), whereas they make an angle of ~15˚ to the [111] direction at 90 K (below the Verwey transition) (Fig. 7d). Figure 7e shows a line profile generated from the magnetic contribution to the phase shift that was used to create Fig. 7c, taken along a line passing through the center of the crystal in a direction perpendicular to the phase contours. A least-squares fit of the experimental phase profile to Eqs 19 and 20 yielded an in-plane magnetic induction $B_{\perp}$ of 0.6(±0.12) T (Harrison et al., 2007). This value is consistent with the room temperature saturation induction of magnetite, suggesting that the magnetization direction of the particle lies in the plane of the specimen, close to the [121] crystallographic direction. This direction corresponds to the longest diagonal dimension of the particle, suggesting that shape anisotropy dominates the magnetic state of the crystal at room temperature. In contrast, the 90 K phase profile yielded a value for $B_{\perp}$ of 0.46(±0.09) T (Harrison et al., 2007). This value is lower than the saturation induction of magnetite at 90 K, suggesting that, at remanence, the magnetization direction in the crystal is tilted out of the plane by ~40° to the horizontal. This direction corresponds approximately to $[100]_{cubic}$ or $[001]_{cubic}$, as expected from the prediction that the $[001]_{monoclinic}$ easy axis can lie along any one of the original $<100>_{cubic}$ directions and that the effect of magnetocrystalline anisotropy on the magnetic state of the crystal is dominant in the monoclinic phase below the Verwey transition (Dunlop & Özdemir, 1997). Ferroelastic twin walls are not observed in crystals of this size.

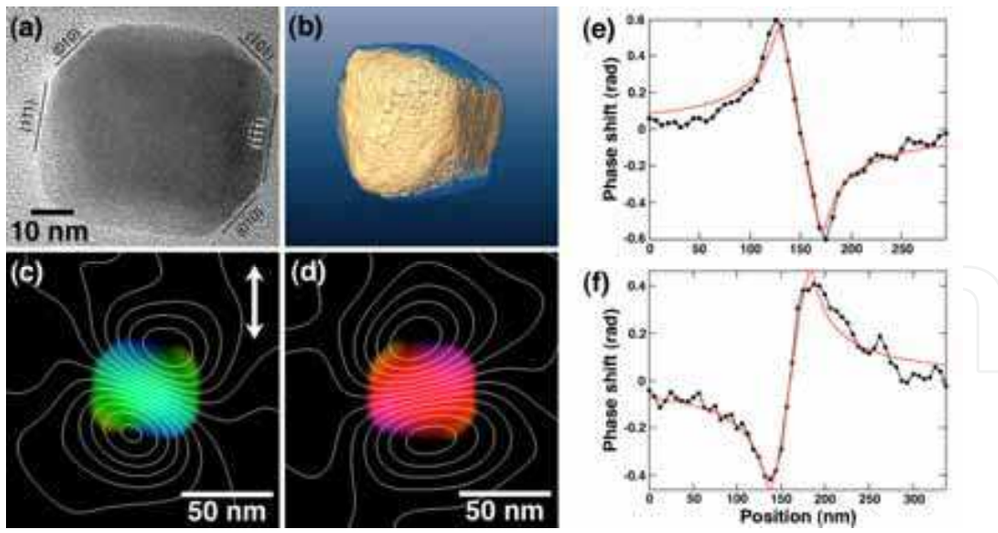

Fig. 7. (a) High-resolution TEM image of a 50-nm-diameter magnetite crystal from a magnetotactic bacterial cell (recorded by M. Pósfai). (b) Three-dimensional morphology of the same particle obtained using high-angle annular dark-field electron tomography (recorded by R.K.K. Chong). (c,d) Remanent magnetic states of the particle recorded at room temperature and at 90 K, respectively. The double arrow shows the applied field direction before reducing the experimental field to zero and recording holograms. (e,f) Data points in the line profiles show the magnetic contribution to the phase shift across the particle measured (e) at room temperature and (f) at 90 K. The red lines show least-squares fits to the data points, yielding values of $B_{\perp}$=0.60(± 0.12) T at room temperature and $B_{\perp}$=0.46(±0.09) T at 90 K.

3.1.1.2 Multi-domain magnetite

Results obtained from a synthetic magnetite specimen with a grain size of 10-30 μm, prepared for TEM using Ar ion milling, are shown in Fig. 8. Figure 8b shows a magnetic induction map recorded at room temperature in magnetic-field-free conditions using electron holography after applying a magnetic field of 2 T to the specimen. The presence of a magnetic flux-closure domain results from the minimization of magnetostatic energy. The magnetic state of this specimen below the Verwey transition (Fig. 8c) is significantly different from that observed at room temperature. At low temperature, the magnetic domains are more complicated and their sizes can be as small as several tens of nm. Magnetic domains that are far from the specimen edge have widths of 100-500 nm and are separated by 180˚ domain walls, which result from the strong uniaxial magnetocrystalline anisotropy of the monoclinic phase (antiparallel magnetization directions are shown in purple and yellow on the right side of Fig. 8c), as predicted in many previous studies (e.g., Dunlop & Özdemir, 1997).

The formation of magnetic domains that are related to "strain-contrast-free" ferroelastic twin walls, which are invisible in conventional TEM images, is depicted in Fig. 8d. The magnetic domain walls appear reproducibly at the same positions after applying large fields to the specimen in opposite directions, suggesting that the positions of the domain walls are defined strictly by underlying crystallographic features. Figure 8e shows a corresponding simulated magnetic induction map generated by using the approach of Beleggia & Zhu (2003), superimposed onto an experimental Lorentz (out-of-focus) TEM image. The crystallographic *c*-axis direction in each domain was determined using electron diffraction, revealing that neighboring monoclinic *c*-axes are at 90˚ to each other. Despite the fact that the parameters used to describe the specimen in the simulation were slightly different from

its true geometry, the simulated image is in good agreement with the experimental magnetic induction map. A small remaining inconsistency in the direction of the phase contours in the purple domains may be caused by specimen thickness variations, stray magnetic fields and/or unknown additional phase ramps in the experimental image. Given that the $[001]_{monoclinic}$ easy axis direction in one of the twin domains points at ~45° out of the specimen plane, the presence of stray fields above and below the sample plane is to be expected. Magnetic structures such as those shown in Fig. 8 are affected significantly by the presence of ferroelastic twins, which therefore play a significant role in determining the unique magnetic properties of magnetite at low temperature (Kasama et al., 2010).

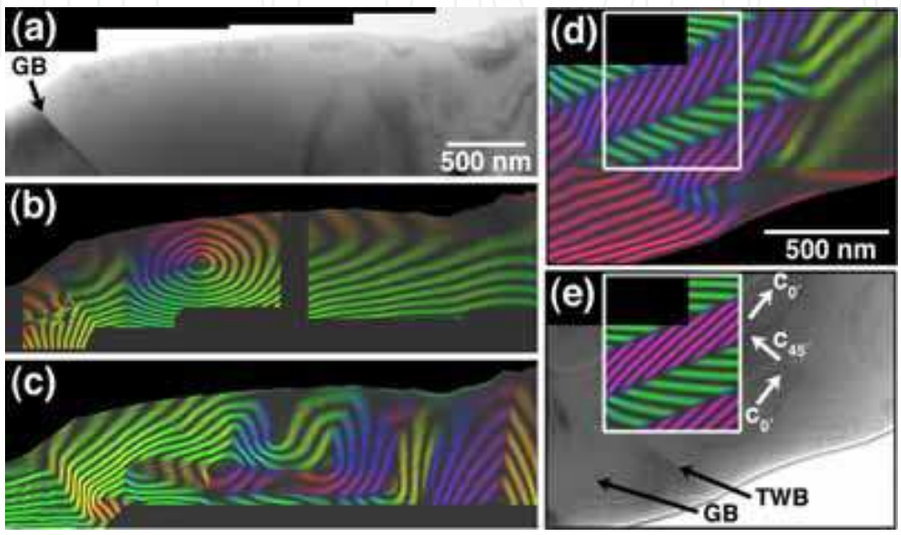

Fig. 8. (a) Bright-field TEM image of a synthetic magnetite specimen. (b,c) Remanent magnetic states recorded using off-axis electron holography at room temperature and below the Verwey transition, respectively. (d) Experimental magnetic induction map recorded from a region containing "strain-contrast-free" ferroelastic twin walls. (e) Simulated induction map superimposed onto an experimental Lorentz TEM image. The parameters used for the simulation were: B=0.6 T, V_0=17 V and a ferroelastic twin domain width of 165 nm. The specimen was assumed to be wedge-shaped with a thickness gradient of 10%. "$c_{0°}$" and "$c_{45°}$" refer to monoclinic c-axes that are oriented in-plane and at an angle of 45˚ to the specimen plane, respectively. The contour spacing is 2π. GB: grain boundary; TWB: twin wall boundary.

3.1.2 Critical size for superparamagnetic behavior in three-dimensional assemblies of magnetite nanoparticles

The particle or grain size is one of the most important parameters that determines the magnetic properties of a material. The effect of particle size and shape on the magnetic state of an isolated magnetite particle was discussed theoretically by Butler & Banerjee (1975), who suggested that the transition from single-domain to superparamagnetic behavior occurs below a particle size of 25-30 nm. Figure 9 shows local magnetic structures of magnetite particle assemblies on smectite (clay) platelets, which provide an ideal geometry for the experimental study of the critical threshold size for superparamagnetic behavior in the presence of strong interactions between adjacent particles (Galindo-Gonzalez et al., 2009). Electron holograms were acquired at remanence using a liquid-nitrogen-cooled TEM specimen holder. Unwanted mean inner potential contributions to the phase were eliminated by using *in situ* magnetization

reversal. Figure 9a shows magnetite particles with an average diameter of ~10 nm, alongside two larger magnetite particles with diameters of 47 and 48 nm. The two larger particles are in close proximity to each other and result in a dipole-like magnetic signal (Fig. 9b). The measured induction in the particles is 0.53 T, which is close to that expected for magnetite (~0.6 T). The smaller particles do not show a detectable magnetic signal. Two agglomerates, each of which contains two touching particles of different size, are shown in Figs 9c and e. The particles in Fig. 9c have diameters of 33 and 42 nm, whereas in Fig. 9e they have diameters of 25 and 32 nm. The agglomerate containing the larger particles shows a magnetic signal (Fig. 9d), whereas the agglomerate with the smaller particles does not (Fig. 9f). This difference provides an estimate of 30–40 nm for the critical threshold size for superparamagnetic behavior in three-dimensional assemblages of magnetite over a timescale of ~10 sec (the time required for hologram collection). It should be noted that stray magnetic fields from larger particles can stabilize the moment of an adjacent smaller particle. An example of such behavior is shown in Figs 9g and h, where the stray field (the return flux) from larger particles appears to stabilize the moments of smaller particles, in the form of a flux-closed magnetic state that would show negligible overall magnetic remanence in a bulk measurement.

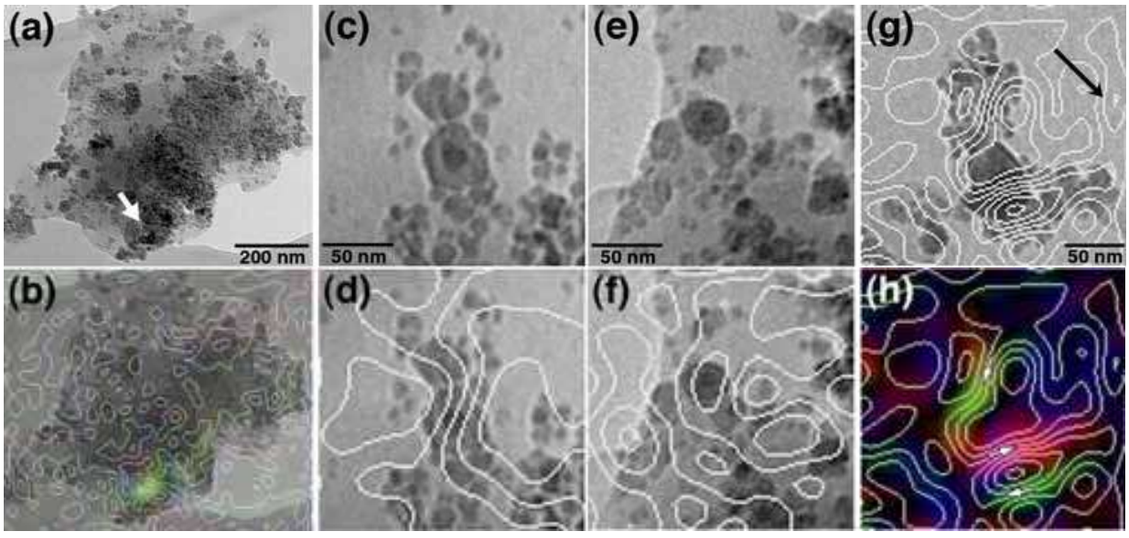

Fig. 9. (a) Bright-field TEM image of magnetite particles adhering to a smectite particle. (b) Corresponding magnetic induction map acquired at 92 K. Two larger crystals next to each other are marked by an arrow in (a). (c-f) Bright-field TEM images of assemblies containing larger, touching particles and corresponding remanent magnetic states. The larger particles in (c) and (d) have diameters of 33 and 42 nm, whereas those in (e) and (f) have diameters of 25 and 32 nm. (g) Magnetic phase contour and color maps recorded at remanence after applying a large field to the specimen in the direction shown with the black arrow in (g). The contour spacing in (b) is 0.125 radians, whereas those in (d), (f), (g) and (h) are 0.0625 radians. Adapted from Galindo-Gonzalez et al. (2009).

3.2 Magnetic thin films

Magnetic thin films are central to the development of spintronic devices such as magnetic random access memories and magnetoresistive read heads. For their development, it is important to characterize their magnetic states and switching field distributions, especially when they take the form of deep-submicron structures. However, most magnetometry techniques lack the sensitivity to characterize individual nanostructures. For example,

although magnetic force microscopy can be used to image stray magnetic fields above samples, it is invasive and cannot be used to measure the magnetization within them.
Here, we illustrate the application of electron holography to the characterization of the magnetic properties of thin films with nanometer spatial resolution. These studies have involved the design and application of a three-contact biasing TEM specimen holder, which allows magnetic devices to be examined under an electrical applied bias in the TEM (Kasama et al., 2005a).

3.2.1 Pseudo-spin-valve thin film elements

A magnetoresistive multilayer typically contains a magnetically hard pinned layer and a magnetically soft free layer, separated by a tunnel barrier or a conducting spacer layer. The resistance of the structure depends on the relative magnetization directions of the two layers. This effect can be used to sense small magnetic fields, which rotate the magnetization direction of the free layer to store a data bit. The sample used in this study comprised a two-dimensional array of 75 × 280 nm pseudo-spin-valve elements, which were prepared from a polycrystalline $Ni_{79}Fe_{21}$ (4.1 nm)/Cu (3 nm)/Co (3.5 nm)/Cu (4 nm) film that had been sputtered onto an oxidized silicon substrate (Kasama et al., 2005b). Figure 10 shows three representative magnetic induction maps recorded from three adjacent elements using electron holography in magnetic-field-free conditions. Figures 10a–c were acquired after saturating the elements upward and then applying external fields with in-plane components of (a) 0 Oe, (b) 424 Oe and (c) 1092 Oe downward. The contours were generated directly from the magnetic contribution to the measured holographic phase shift, after subtracting the mean inner potential contribution from each recorded phase image using *in situ* magnetization reversal. Where the phase contours in the elements are closely-spaced, the directions of the two magnetic layers are inferred to be parallel, whereas where the contours are widely-spaced the magnetic layers are inferred to be antiparallel. The magnetic configurations do not have end domains or vortices, and magnetic interactions between the neighboring elements are not significant.

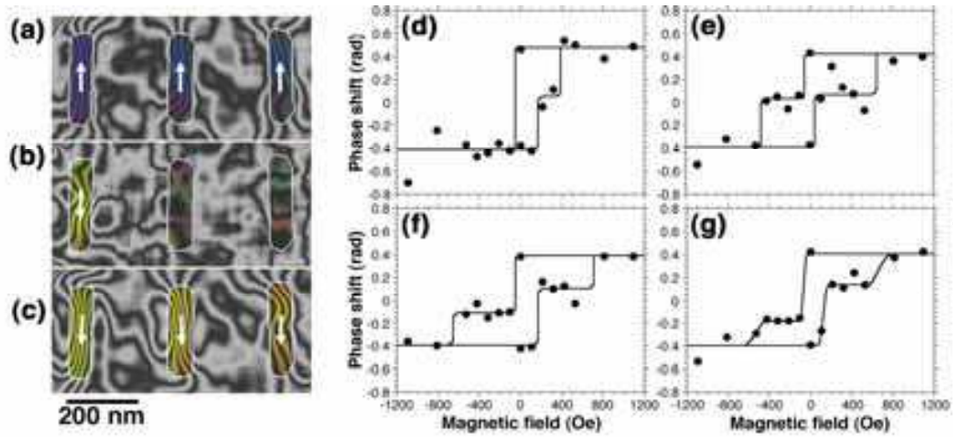

Fig. 10. (a-c) Magnetic induction maps recorded at remanence from three pseudo-spin-valve elements, after saturating the elements upwards and then applying external fields with in-plane components of (a) 0 Oe, (b) 424 Oe and (c) 1092 Oe downwards. The arrows show the local magnetization directions. The phase contour spacing is 0.098 radians. (d-g) Remanent hysteresis loops measured from each of the three elements shown in (a)-(c). The loops in (d), (e), (f) and (g) were obtained from the left, middle and right elements and their average, respectively. Adapted from Kasama et al. (2005b).

Remanent hysteresis loops measured from the magnetic contributions to the recorded phase images for each of the three elements are shown in Figs 10d-g. Figure 10d shows an antiparallel state in only one direction, with switching fields for the two layers of 100-200 and 100-400 Oe. In comparison, the other elements have switching fields of 100–200 and 500-700 Oe. Such switching variability is consistent with a collective hysteresis loop measured from ~10^9 elements, in which the switching field variations of the NiFe and Co layers are 50 and 150 Oe, respectively (Kasama et al., 2005b). The width of the switching field distribution is thought to result from variations in the shapes and sizes of the elements and from microstructural variability, which must be minimized if such elements are to be used in ultra-high-areal-density magnetic recording applications.

3.2.2 Magnetite thin film containing anti-phase domains

Magnetite is a promising candidate for spintronic applications because it is expected to be an efficient source of spin-polarised electrons. In layered magnetite films, it has been suggested that unexpectedly low magnetoresistance may result from the presence of antiferromagnetic coupling at anti-phase domain boundaries (APBs) (Fig. 11a), which would randomize the spins of conduction electrons. We have used electron holography to examine magnetic remanent states in an (001) magnetite thin film that was grown epitaxially on MgO and contains APBs (Kasama et al., 2006a). The magnetic induction maps that are shown in Figs 11b and d were acquired after saturating the sample magnetically downward and then applying fields with components in the plane of the sample of 192 and 513 Oe upward, respectively. The colors indicate the direction of the measured induction, according to the color wheel shown in Fig. 11c. In contrast to the examination of patterned magnetic nanostructures and nanocrystals, the mean inner potential contribution did not have to be subtracted from each recorded phase image because the film thickness was uniform across the field of view. The thin red and blue lines on each magnetic induction map correspond to the positions of the APBs that are visible in dark-field images obtained using 220 and 131 reflections, respectively. White lines correspond to the APBs that are visible using both reflections.

Although the remanent magnetic states are highly complicated, two types of magnetic domain contrast can be seen (Fig. 11b): (i) coarse magnetic domains (typically 100-350 nm in size) and (ii) finer magnetic domains (typically 10-90 nm in size). Adjacent coarse domains differ in their average magnetization direction by approximately 90° or 180˚. Each coarse domain contains fluctuations in magnetization direction that occur on a scale similar to the size of the anti-phase domains. In Fig. 11d, antiferromagnetic coupling is visible as a 180˚ change in the local magnetic induction direction across several APBs, as indicated in the boxed region. The APBs that exhibit antiferromagnetic coupling are typically associated with a strong out-of-plane component of the magnetization in the film. Figure 11e shows the variation of the inclination of the magnetization from the plane of the film, inferred from the measured in-plane component of the magnetic induction and plotted as a function of distance from a single APB in Fig. 11d. The local moments at the position of the APB are inclined at an angle of almost 90˚ to the plane of the specimen, gradually rotating back to the specimen plane over a distance of ~17 nm. Our observations suggest that the magnetic properties of the magnetite thin film are related strongly to local crystallographic features at the positions of APBs. However, antiferromagnetic coupling is not present at each APB and the low value of magnetoresistance is unlikely to be explained by their presence alone (Kasama et al., 2006a).

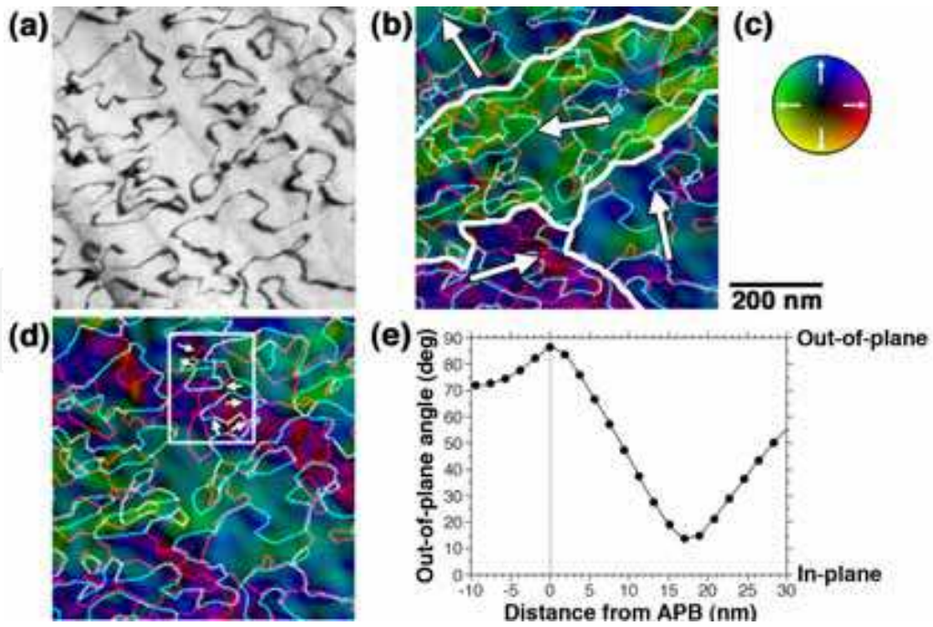

Fig. 11. (a) Dark-field image acquired using the 131 reflection of magnetite, showing APBs in a 25-nm-thick (001) magnetite thin film grown epitaxially on MgO. (b,d) Magnetic remanent states acquired from the region shown in (a), after saturating the film downward magnetically and then applying fields with in-plane components of 192 and 513 Oe upward, respectively. The arrows in (b) indicate the average magnetic induction direction in each coarse magnetic domain. The arrows in (d) show the local magnetic induction directions associated with antiferromagnetic coupling at APBs. The thin red, blue and white lines mark the positions of APBs. (c) Color wheel, representing the magnetic induction directions in (b) and (d). (e) Measured variation of the inclination of the magnetization from the plane of the film plotted as a function of distance from an APB. Adapted from Kasama et al. (2006a).

3.2.3 Current-induced motion of magnetic domain walls in permalloy wires

It has recently been demonstrated that spin-transfer effects associated with injected currents can be used to displace magnetic domain walls (Saitoh et al., 2004). This effect is of interest for the development of novel memory and logic devices based on domain-wall propagation (Allwood et al., 2002). A combination of Lorentz TEM and electron holography can be used to study the motion of magnetic domain walls induced by currents (Junginger et al., 2007) by using an electrical biasing TEM specimen holder, as described above. Here, permalloy zigzag line structures with a line width and thickness of 430 and 11 nm, respectively were fabricated on electron-transparent SiN windows using electron-beam lithography, as shown in Fig. 12a. Figure 12b shows the sequential positions of a domain wall that was subjected to 10 μs pulses with a current density of 3.14×10^{11} A/m^2. Electron holograms were acquired at each of these positions. It was observed that a transverse wall initially formed at a kinked region of the wire after the application of a magnetic field. After applying a current pulse, the domain wall moved by 2330 nm in the direction of electron flow and transformed into a vortex-type domain wall. After a second pulse, the vortex domain wall moved slightly in the same direction and became distorted (3 in Fig. 12b), with the long axis of the vortex inclined increasingly perpendicular to the wire length. This behavior may be associated with edge

roughness or defects, which often restrict magnetic wall movements. After the third pulse, the domain wall moved by a further 260 nm and retained a vortex state. More recent studies have involved the injection of small currents to influence thermally-activated magnetic domain wall motion between closely-adjacent pinning sites (Eltschka et al., 2010).

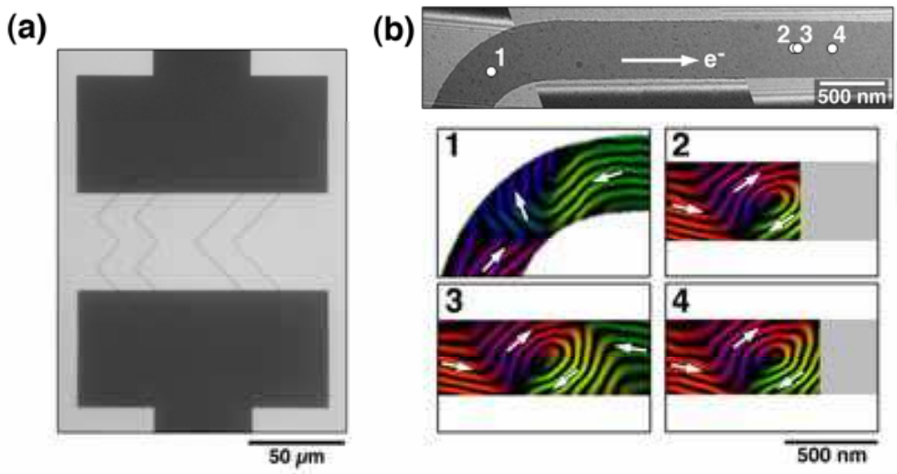

Fig. 12. (a) Low-magnification TEM image of four permalloy zigzag wires (width: 430 nm, thickness: 11 nm) patterned onto a SiN window using electron-beam lithography. A kink in one wire was examined using electron holography. (b) Higher-magnification TEM image of a permalloy wire, showing the motion of a domain wall after the injection of 10 μs pulses with a current density of 3.14×10^{11} A/m^2, showing magnetic induction maps obtained from a domain wall at each position. The long arrow in the top image indicates the direction of electron flow. The phase contour spacing is 0.785 radians.

3.3 Magnetotactic bacteria

Magnetotactic bacteria comprise a number of aquatic species that migrate along geomagnetic field lines. This behavior results from the presence of intracellular magnetic crystals of magnetite or greigite (Fe_3S_4). Similar magnetic crystals are also found in other organisms, such as fish, birds and humans, although their function is often poorly understood (Pósfai & Dunin-Borkowski, 2009). Here, we use electron holography to study the magnetic microstructures of greigite crystals in magnetotactic bacteria that contain multiple chains of either slightly elongated or almost equidimensional crystals (Kasama et al., 2006b).

A magnetic induction map recorded using off-axis electron holography from a dividing bacterial cell is shown in Figure 13. The cell contains several highly-elongated magnetite crystals alongside 50-nm-diameter greigite crystals. The measured magnetic induction approximately follows the distribution of greigite crystals in the multiple chain (Fig. 13). However, there are considerable variations in the local direction of the induction within individual particles, presumably as a result of variations in their morphology and orientation. In general, the more elongated crystals appear to be more strongly magnetic, particularly if the elongation and chain axes are parallel to each other. However, several crystals in the outer regions of the chain either appear to be non-magnetic or their induction elongation are parallel to the elongation of the crystal rather than to the chain axis. The crystals that appear to be non-magnetic may be magnetized largely out of the plane of the

specimen, since electron holography is only sensitive to the in-plane components of the magnetic induction. Overall, shape anisotropy appears to be the most important factor controling the magnetization direction of each crystal (unless they are very closely-spaced), followed by interparticle interactions, whereas magnetocrystalline anisotropy is the least important. Although the crystals in the cell are less well organized with respect to their morphology, crystallographic orientation and position, when compared with magnetite-producing bacteria, they provide a measured collective magnetic moment (~9 x 10^{-16} Am^2) that is sufficient for magnetotaxis and is calculated to allow the cell to migrate along geomagnetic field lines at more than 90% of its forward speed. The magnetic moment and forward speed were determined using methods described by Dunin-Borkowski et al. (1998) and Frankel (1984), respectively. These results provide new insight for understanding magnetotaxis in iron sulfide-producing magnetotactic bacteria.

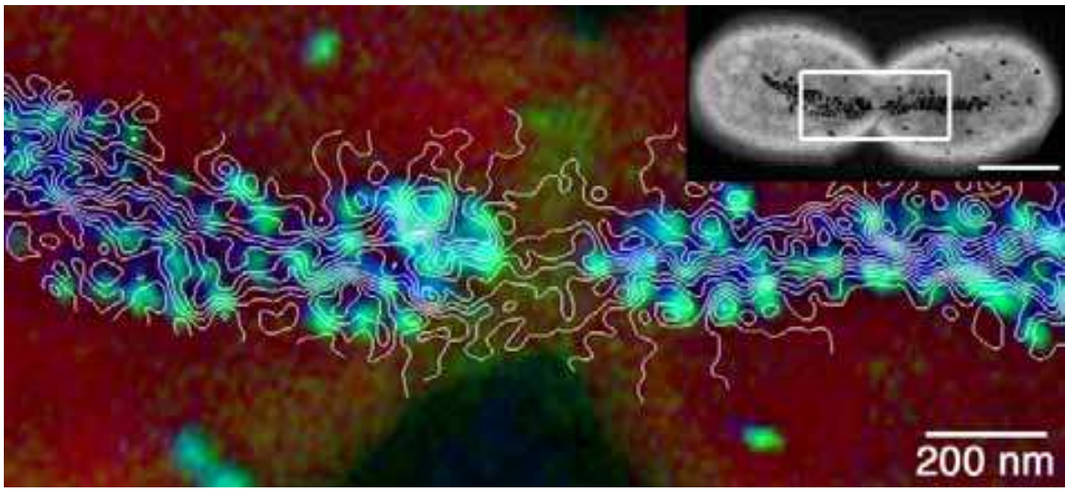

Fig. 13. Magnetic induction map recorded from greigite (Fe_3S_4) and magnetite (Fe_3O_4) crystals in a dividing magnetotactic bacterial cell using off-axis electron holography, superimposed onto an elemental map (red: carbon, green: sulfur, blue: iron). The rounded greigite crystals (light blue) are covered by an amorphous iron oxide (darker blue). The phase contour spacing is 0.098 radians. A carbon map of the entire dividing cell is shown in the inset (the scale bar is 1 μm). The box indicates the region from which the magnetic induction map was obtained. Adapted from Kasama et al. (2006b).

4. Quantitative measurement of magnetic moments using electron holography

The magnetic moment of a nanostructure is given by the expression

$$m = \iiint \mathbf{M}(\mathbf{r}) d^3 r \tag{27}$$

where $\mathbf{M}(\mathbf{r})$ is the position-dependent magnetization and $\mathbf{r}$ is a three-dimensional position vector. Unfortunately, a holographic phase image does not provide direct information about $\mathbf{M}(\mathbf{r})$. Instead, the recorded phase shift is proportional to the projection (in the beam direction) of the in-plane components of the magnetic induction $\mathbf{B}(\mathbf{r})$ both within and around the specimen. We have recently shown mathematically that the magnetic moment of a nanostructure can in fact be measured quantitatively from a phase image or its gradient

components (Beleggia et al., 2010). The basis of the algorithm is the relationship between the volume integral of the magnetic induction, a quantity that is referred to here as the "inductive moment" $\mathbf{m_B}$ and the magnetic moment. If a circular boundary around an isolated nanostructure of interest is chosen when integrating the phase shift in the form

$$\mathbf{m_B} = \frac{\hbar R}{e\mu_0}\int_0^{2\pi} d\theta[-\sin\theta, \cos\theta, 0]\phi(R\cos\theta, R\sin\theta) \tag{28}$$

where R is the radius of the integration circle, μ_0 is the vacuum permeability and θ is the polar angle. Then the following expression is found to be valid:

$$\mathbf{m} = 2\mathbf{m_B}\,. \tag{29}$$

Furthermore, two orthogonal components of $\mathbf{m_B}$ can be extrapolated as a function of the radius of the integration circle to a circle of zero radius to yield a measurement that is free of most artifacts (see Beleggia et al. (2010) for details).

In order to demonstrate the applicability of this approach to experimental phase images, we measured the magnetic moment of a chain of three closely-spaced magnetite crystals from a magnetotactic bacterium (Fig. 14a). The gradient of the magnetic contribution to the recorded phase shift is integrated within circles with radii of 100 to 240 nm in 1 nm increments (Fig. 14b). The two components of the inductive moment that are calculated from each measurement are extrapolated quadratically to zero circle radius, as shown in Fig. 14c. The best-fitting value for the measured inductive moment is 2.74(±0.18)×10^6 μ_B oriented at 136(±4)°. The magnetization obtained from the inductive moment and the volume of the three crystals is 510(±90) kA/m, which is in good agreement with that expected for magnetite, 480 kA/m.

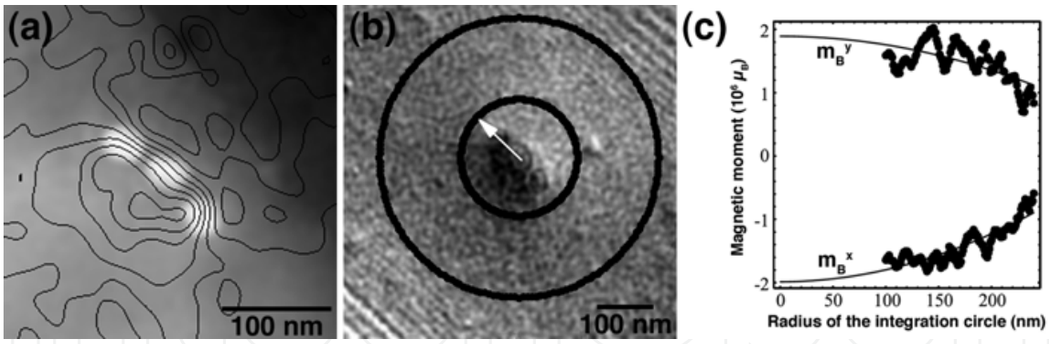

Fig. 14. (a) Magnetic induction map acquired using electron holography from three magnetite crystals in a bacterial cell. The phase contour spacing is 0.0625 radians. (b) Magnetic contribution to the phase shift corresponding to (a). The circles and arrow show integration radii of 100 and 240 nm and the direction of the measured inductive moment determined by extrapolating the measurements quadratically to zero integration radius, as shown in (c). Adapted from Beleggia et al. (2010).

5. Conclusions

In combination with TEM techniques that allow crystallographic and compositional information about materials to be obtained at atomic resolution, off-axis electron

holography provides a powerful tool for the study of nanometer-scale magnetic fields in materials and devices, especially if advanced TEM specimen holders are used to apply external stimuli for studying processes such as current-induced domain wall motion.

The phase sensitivity and spatial resolution of off-axis electron holography have been discussed by de Ruijter & Weiss (1993), who suggested that a practical phase sensitivity of $2\pi/100$ radians can be achieved by using digital recording and image processing. In magnetic samples, this sensitivity corresponds to a detectable signal from a ~6 nm particle with a magnetization similar to that of cobalt (1.8 T). In the future, a phase sensitivity of $2\pi/1000$ radians and a spatial resolution of a few nanometers may be required for studies of spintronic devices such as diluted magnetic semiconductors and self-assembled nanostructured devices. Such experiments will require the use of high-brightness electron sources, aberration correctors, highly sensitive recording media, drift-free specimen stages and holders and sophisticated software for the automation of lengthy experiments. In addition, novel image analysis and model-based algorithm will be necessary to enhance weak magnetic signals.

One of the major limitations of electron holography is that it is currently only able to image the *projection* of the in-plane magnetic field onto the two-dimensional sample plane. The combination of electron holography with electron tomography would allow three-dimensional magnetic vector fields inside nanostructured materials to be visualized by applying suitable reconstruction techniques to ultra-high-tilt series of electron holograms acquired about orthogonal specimen-tilt axes (Lai et al., 1994). The practical achievement of magnetic vector field tomography is an attractive prospect, as it would lead to the complete characterization of the magnetic field inside real nanostructured materials and devices that have three-dimensional shapes and distributions.

6. Acknowledgment

We are grateful to R.K.K. Chong, N.S. Church, J.M. Feinberg, R.J. Harrison, J.R. Jinschek, M. Kläui, E.T. Simpson, M. Pósfai and other colleagues for the provision of samples and for ongoing collaborations. The electron holography described here was carried out at the Electron Microscopy group, University of Cambridge and the Center for Electron Nanoscopy, Technical University of Denmark.

7. References

Allwood, D.A.; Xiong, G.; Cooke, M.D.; Faulkner, C.C.; Atkinson, D.; Vernier, N. & Cowburn, R.P. (2002). Submicrometer ferromagnetic NOT gate and shift register. Science 296, 2003-2006.

Beleggia, M. & Zhu, Y. (2003). Electron-optical phase shift of magnetic nanoparticles: I. Basic concepts. Philos. Mag. 83, 1045–1057.

Beleggia, M.; Kasama, T. & Dunin-Borkowski, R.E. (2010) The quantitative measurement of magnetic moments from phase images of nanoparticles and nanostructures - I. Fundamentals. Ultramicroscopy 110, 425-432.

Butler, R.F. & Banerjee, S.K. (1975). Theoretical single-domain grain size range in magnetite and titanomagnetite. J. Geophys. Res. 80, 4049-4058.

Cooper, D.; Truche, R.; Rivallin, P.; Hartmann, J-M.; Laugier, F.; Bertin, F.; Chabli, A. & Rouviere, J-L. (2007). Medium resolution off-axis electron holography with millivolt sensitivity. Appl. Phys. Lett. 91, 143501.

Cowley, J.M. (1992). Twenty forms of electron holography. Ultramicroscopy 41, 335-348.

Cowley, J.M. & Spence, J.C.H. (1998). Principles and theory of electron holography, In: Introduction to Electron Holography, E. Völkl, L.F. Allard & D.C. Joy (Eds), pp.17-56, Kluwer Academic/Plenun Publishers, New York.

de Graef, M., Nuhfer NT, McCartney, MR. (1999) Phase contrast of spherical magnetic particles. J. Microsc. 194, 84-94.

de Ruijter, W.J. & Weiss, J.K. (1993) Detection limits in quantitative off-axis electron holography. Ultramicrscopy 50, 269-283.

Dunin-Borkowski, R.E.; McCartney, M.R.; Frankel, R.B.; Bazylinski, D.A.; Pósfai, M. & Buseck, P.R. (1998). Magnetic microstructure of magnetotactic bacteria by electron holography. Science 282, 1868-1870.

Dunin-Borkowski, R.E.; McCartney, M.R. & Smith, D.J. (2004). Electron holography of nanostructured materials, In: H.S. Nalwa (Ed.), Encyclopedia of Nanoscience and Nanotechnology, Vol. 3, pp.41-100, American Scientific Publishers.

Dunlop, D.J. & Özdemir, Ö. (1997). Rock magnetism: Fundamentals and frontiers, Cambridge University Press, Cambridge.

Egerton, R.F. (1996). Electron energy-loss spectroscopy in the electron microscope (2nd edition), Plenum, New York.

Eltschka, M.; Wötzel, M.; Rhensius, J.; Krzyk, S.; Nowak, U.; Kläui, M.; Kasama, T.; Dunin-Borkowski, R.E.; Heyderman, L.J.; van Driel, H. J. & Duine, R.A. (2010). Nonadiabatic spin torque investigated using thermally activated magnetic domain wall dynamics. Phys. Rev. Lett. 105, 056601.

Erni, R.; Rossell, M.D.; Kisielowski, C. & Dahmen, U. (2009). Atomic-resolution imaging with a sub-50-pm electron probe. Phys. Rev. Lett., 102, 096101.

Frankel, R.B. (1984). Magnetic guidance of organisms. Ann. Rev. Biophys. Bioeng. 13, 85-103.

Frost, B.G.; Völkl, E & Allard, L.F. (1996). An improved mode of operation of a transmission electron microscope for wide field off-axis holography. Ultramicrscopy 63, 15-20.

Gabor, D. (1949). Microscopy by reconstructed wave-fronts. Proc. Roy. Soc. A 197, 454-487.

Galindo-Gonzalez, C.; Feinberg, J.M.; Kasama, T.; Cervera-Gontard, L.; Pósfai, M.; Kósa, I.; Duran, J.D.G.; Gil, J.E.; Harrison, R.J. & Dunin-Borkowski, R.E. (2009). Magnetic and microscopic characterization of magnetic nanoparticles adhered to clay surfaces. Am. Mineral. 94, 1120-1129.

Haine, M.E. & Mulvey, T. (1952). The formation of the diffraction image with electrons in the Gabor diffraction microscope. J. Opt. Soc. Am. 42, 763-769.

Harada, K.; Akashi, T.; Togawa, Y.; Matsuda, T. & Tonomura, A. (2005). Optical system for double-biprism electron holography. J Electron Microsc. 54, 19-27.

Harada, K.; Matsuda, T.; Tonomura, A.; Akashi, T. & Togawa, Y. (2006). Triple-biprism electron interferometry. J. Appl. Phys. 99, 113502.

Harrison, R.J.; Dunin-Borkowski, R.E.; Kasama, T.; Simpson, E.T. & Feinberg, J.M. (2007). Magnetic properties of rocks and minerals, In: Treatise on Geophysics, Vol. 2, G. Schubert (Ed.), pp.579-630, Elsevier Science.

Junginger, F.; Kläui, M.; Backes, D.; Rüdiger, U.; Kasama, T.; Dunin-Borkowski, R.E.; Heyderman, L.J.; Vaz, C.A.F. & Bland, J.A.C. (2007). Spin torque and heating effects in current-induced domain wall motion probed by transmission electron microscopy. Appl. Phys. Lett. 88, 212510.

Kasama, T.; Dunin-Borkowski, R.E.; Matsuya, L.; Broom, R.F.; Twitchett, C.A.; Midgley, P.A.; Newcomb, S.B.; Robins, A.C.; Smith, D.W.; Gronsky, J.J.; Thomas, C.A. & Fischione, P.E. (2005a). A versatile three-contact electrical biasing transmission electron microscope specimen holder for electron holography and electron tomography of working devices. In In-situ Electron Microscopy of Materials, Vol. 907E, P.J. Ferreira, I.M. Robertson, G. Dehm, and H. Saka (Eds), Materials Research Society, Pittsburgh, PA, pp. MM13-02.

Kasama, T.; Barpanda, P.; Dunin-Borkowski, R.E.; Newcomb, S.B.; McCartney, M.R.; Castaño, F.J. & Ross, C.A. (2005b). Off-axis electron holography of individual pseudo-spin-valve thin film magnetic elements. J. Appl. Phys. 98, 013903.

Kasama, T.; Dunin-Borkowski, R.E. & Eerenstein, W. (2006a). Off-axis electron holography observation of magnetic microstructure in a magnetite (001) thin film containing antiphase domains. Phys. Rev. B 73, 104432.

Kasama, T.; Pósfai, M.; Chong, R.K.K.; Finlayson, A.P.; Buseck, P.R.; Frankel, R.B. & Dunin-Borkowski, R.E. (2006b). Magnetic properties, microstructure, composition and morphology of greigite nanocrystals in magnetotactic bacteria from electron holography and tomography. Amer. Mineral. 91, 1216-1229.

Kasama, T.; Dunin-Borkowski, R.E.; Scheinfein, M.R.; Tripp, S.L.; Liu, J. & Wei, A. (2007). Off-axis electron holography of self-assembled Co nanoparticle rings. In: Quantitative Electron Microscopy for Materials Science, Vol. 1026E, E. Snoeck, R.E. Dunin-Borkowski, J. Verbeeck & U. Dahmen (Eds), Materials Research Society, Warrendale, PA, pp. C18-03.

Kasama, T.; Dunin-Borkowski, R.E.; Scheinfein, M.R.; Tripp, S.L.; Liu, J. & Wei, A. (2008). Reversal of flux closure states in cobalt nanoparticle rings with coaxial magnetic pulses. Adv. Mater. 20, 4248-4252.

Kasama, T.; Church, N.; Feinberg, J.M.; Dunin-Borkowski, R.E. & Harrison, R.J. (2010). Direct observation of ferromagnetic/ferroelastic domain interactions in magnetite below the Verwey transition. Earth Planet. Sci. Lett. 297, 10-17.

Lai, G.; Hirayama, T.; Ishizuka, K. & Tonomura, A. (1994). Three-dimensional reconstruction of electric-potential distribution in electron-holographic interferometry, J. Appl. Opt. 33, 829–833.

Lehmann, M.; Lichte, H.; Geiger, D.; Lang, G. & Schweda, E. (1999). Electron holography at atomic dimensions – present state. Mater. Character. 42, 249-263.

Lichte, H. (1991). Electron image plane off-axis electron holography of atomic structures. Adv. Opt. Electron Microsc. 12, 25-91.

Lichte, H. (1996). Electron holography: optimum position of the biprism in the electron microscope. Ultramicroscopy 64, 79-86.

Lichte, H. (2008). Performance limits of electron holography. Ultramicroscopy 108, 256-262.

Loudon, J.C.; Mathur, N.D. & Midgley, P.A. (2002). Charge-ordered ferromagnetic phase in $La_{0.5}Ca_{0.5}MnO_3$. Nature 420, 797-800.

Matsuda, T.; Hasegawa, S.; Igarashi, M.; Kobayashi, T.; Naito, M.; Kajiyama, H.; Endo, J.; Osakabe, N.; Tonomura, A. & Aoki, R. (1989). Magnetic field observation of a single flux quantum by electron-holographic interferometry. Phys. Rev. Lett. 62, 2519-2522.

Möllenstedt, G. & Düker, H. (1956). Beobachtungen und messungen an biprisma-interferenzen mit electronenwellen. Z. Physik 145, 377-397.

Pankhurst, Q.A.; Thanh, N.K.T.; Jones, S.K. & Dobson, J. (2009) Progress in applications of magnetic nanoparticles in biomedicine. J. Phys. D: Appl. Phys. 42, 224001.

Phatak, C.; Bain, J.A.; Zhu, J.G. & De Graef, M. (2008). Aberration corrected Lorentz microscopy for perpendicular magnetic recording media. Microsc. Microanal. 14, 832-833.

Pósfai, M & Dunin-Borkowski, R.E. (2009). Magnetic nanocrystals in organisms. Elements 5, 235-240.

Saitoh, E.; Miyajima, H.; Yamaoka, T. & Tatara, G. (2004). Current-induced resonance and mass determination of a single magnetic domain wall. Nature 432, 203-206.

Sickmann, J.; Formanek, P.; Linck, M.; Muehle, U. & Lichte, H. (2011). Imaging modes for potential mapping in semiconductor devices by electron holography with improved lateral resolution. Ultramicroscopy 111, 290-302.

Smirnov, A.V. & Tarduno, J.A. (2002). Magnetic field control of the low temperature magnetic properties of stoichiometric and cation-deficient magnetite. Earth Planet. Sci. Lett. 194, 359-368.

Smith, D.J. (2007). Characterisation of nanomaterials using transmission electron microscopy, In: Nanocharacterisation, A.I. Kirkland & J.L. Hutchison (Eds), pp.1-27, RSC Publishing, Cambridge.

Smith, D.J. & McCartney, M.R. (1998). Practical electron holography, In: Introduction to Electron Holography, E. Völkl, L.F. Allard & D.C. Joy (Eds), pp.87-106, Kluwer Academic/Plenun Publishers, New York.

Takeda, M.; Ina, H. & Kobayashi, S. (1982). Fourier-transform method of fringe-pattern analysis for computer-bases topography and interferometry. J. Opt. Soc. Am. 72, 156-160.

Tonomura, A. (1992). Electron-holographic interference microscopy. Adv. Phys. 41, 59-103.

Tonomura, A; Osakabe, N; Matsuda, T.; Kawasaki, T.; Endo, J.; Yano, S. & Yamada, H. (1986). Evidence for Aharonov-Bohm effect with magnetic field completely shielded from electron wave. Phys. Rev. Lett. 56, 792-795.

Verbeeck, J.; Bertoni, G. & Lichte, H. (2011). A holographic biprism as a perfect energy filter? Ultramicroscopy 111, 887-893.

Verwey, E.J.W. (1939). Electronic conduction of magnetite (Fe_3O_4) and its transition point at low temperature. Nature 144, 327-328.

Völkl, E & Lichte, H. (1990). Electron holograms for subångström point resolution. Ultramicroscopy 32, 177-180.

Völkl, E.; Allard, L.F.; Datye, A. & Frost, B.G. (1995). Advanced electron holography: a new algorithm for image processing and a standardized quality test for the FEG electron microscope. Ultramicroscopy 58, 97-103.

Walz, F. (2002). The Verwey transition - a topical review. J. Phys. Cond. Matter. 14, R285-R340.

Yamamoto, K.; Hirayama, T. & Tanji, T. (2004). Off-axis electron holography without Fresnel fringes. Ultramicroscopy 101, 265-269.

IntechOpen

IntechOpen

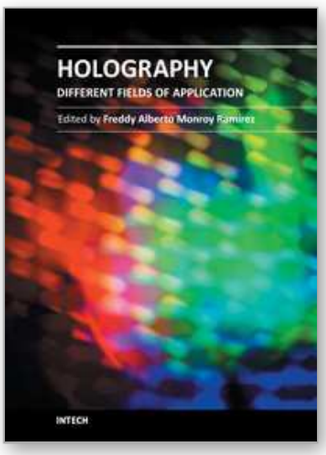

Holography - Different Fields of Application

Edited by Dr. Freddy Monroy

ISBN 978-953-307-635-5
Hard cover, 148 pages
Publisher InTech
Published online 12, September, 2011
Published in print edition September, 2011

This book depicts some differences from the typical scientific and technological literature on the theoretical study of holography and its applications. It offers topics that are not very commercial nor known, which will allow a different view of the field of optics. This is evident in chapters such as â€œElectron Holography of Magnetic Materialsâ€, â€œPolarization Holographic Gratings in Polymer Dispersed Formed Liquid Crystals, and â€œDigital Holography: Computer-generated Holograms and Diffractive Optics in Scalar Diffraction Domainâ€. The readers will gain a different view of the application areas of holography and the wide range of possible directions that can guide research in the fields of optics.

How to reference

In order to correctly reference this scholarly work, feel free to copy and paste the following:

Takeshi Kasama, Rafal E. Dunin-Borkowski and Marco Beleggia (2011). Electron Holography of Magnetic Materials, Holography - Different Fields of Application, Dr. Freddy Monroy (Ed.), ISBN: 978-953-307-635-5, InTech, Available from: http://www.intechopen.com/books/holography-different-fields-of-application/electron-holography-of-magnetic-materials

INTECH
open science | open minds

InTech Europe
University Campus STeP Ri
Slavka Krautzeka 83/A
51000 Rijeka, Croatia
Phone: +385 (51) 770 447
Fax: +385 (51) 686 166
www.intechopen.com

InTech China
Unit 405, Office Block, Hotel Equatorial Shanghai
No.65, Yan An Road (West), Shanghai, 200040, China
中国上海市延安西路65号上海国际贵都大饭店办公楼405单元
Phone: +86-21-62489820
Fax: +86-21-62489821

© 2011 The Author(s). Licensee IntechOpen. This chapter is distributed under the terms of the Creative Commons Attribution-NonCommercial-ShareAlike-3.0 License, which permits use, distribution and reproduction for non-commercial purposes, provided the original is properly cited and derivative works building on this content are distributed under the same license.

IntechOpen

IntechOpen